

www.acsaem.org Article

# Spectroscopic Characterization of Highly Active Fe-N-C Oxygen Reduction Catalysts and Discovery of Strong Interaction with Nafion Ionomer

Roman Ezhov, Olga Maximova, Xiang Lyu, Denis Leshchev, Eli Stavitski, Alexey Serov, and Yulia Pushkar\*



Cite This: https://doi.org/10.1021/acsaem.3c02522



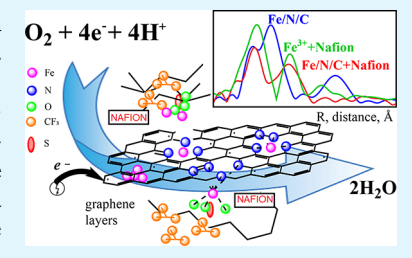
**ACCESS** I

III Metrics & More

Article Recommendations

Supporting Information

**ABSTRACT:** Scaling up clean-energy applications necessitates the development of platinum group metal (PGM)-free fuel cell electrocatalysts with high activity, stability, and low cost. Here, X-ray absorption (XAS) at the Fe K-edge and Fe  $K_{\beta}$  X-ray emission (XES) spectroscopies were used to study the electronic structure of Fe centers in highly active Fe–N–C oxygen reduction catalysts with significant commercial potential. X-ray absorption near-edge structure (XANES) analysis has shown that the majority (>95%) of Fe centers are in the Fe<sup>3+</sup> oxidation state, while extended X-ray absorption fine structure (EXAFS) detected a mixture of single site Fe–N<sub>4</sub> centers (>95%) and centers with short (~2.5 Å) Fe–Fe interactions of Fe metal and/or Fe-carbide nanoparticles (<5%) featuring the Fe<sup>0</sup> oxidation



state. Surprisingly, addition of Nafion, the most widely used ionomer, resulted in pronounced changes in the XAS spectra, consistent with a strong catalyst–ionomer interaction where long Fe–Fe interactions at  $\sim$ 3.1 Å were shown to be a feature of Fe<sup>3+</sup> ions bound with the Nafion. We conclude that exposure to Nafion during the device formulation has a different effect from the aggressive acid leaching typically used in the preparation of Fe–N–C catalysts. It was hypothesized that the polymer interacts with single sites' Fe<sup>3+</sup> centers, as well as with graphene layers protecting the Fe<sup>0</sup> nanoparticles, and extracts some Fe ions into the Nafion matrix.

**KEYWORDS:** Fe-N-C catalyst, earth-abundant fuel cell catalyst, oxygen reduction reaction, X-ray emission spectroscopy, X-ray absorption spectroscopy

### 1. INTRODUCTION

Driven by increasing demands for renewable clean energy and concerns about environmental pollution, enormous efforts have been devoted to exploring new, green, and sustainable energy sources.<sup>1,2</sup> Hydrogen is not only the most abundant element in the universe but also the cleanest fuel on the earth, and it possesses a high energy density (120 MJ kg<sup>-1</sup>, three times higher than that of gasoline) with only an exhaust product of water.<sup>3-5</sup> Currently, H<sub>2</sub> is mainly produced from fossil fuels (e.g., natural gas reforming, petroleum fractionation, and coal gasification). <sup>6-8</sup> Therefore, fossil fuel-based hydrogen production is nonrenewable, and its byproducts—the greenhouse effect, acidic rain, ozone holes, and airborne fine particulate matter—are environmentally hazardous. 9,10 Consequently, green H<sub>2</sub> produced using renewable energy (such as wind, tidal, and solar) has been considered a potential alternative to fossil fuels, as it could address both the energy shortage and environmental pollution caused by fossil fuels. 11,12 Among various energy-conversion technologies powered by H2, such as solid-oxide fuel cells (SOFCs), alkaline-exchange membrane fuel cells (AEMFCs), and proton-exchange membrane fuel cells (PEMFCs), PEMFCs are more promising due to their easy fabrication, low operation temperature, high efficiency, and technology maturity. 13,14 PEMFCs can directly convert the chemical energy released in the reaction of H<sub>2</sub> with O<sub>2</sub> into electrical energy via the hydrogen oxidation reaction (HOR) and oxygen reduction reaction (ORR), at the anode and cathode, respectively, and they can be used for transportation, portable, and stationary applications. Platinum (Pt) group metals (PGMs) are state-ofthe-art electrocatalysts for HOR and ORR. Unfortunately, the high overall stack cost is the predominant factor limiting the large-scale deployment of PEMFCs, 15-20 and PGMs are the main stack cost contributor—around 46%—due to their high cost and limited reserve.<sup>21</sup> The ORR at the cathode is inherently more sluggish by 6 orders of magnitude compared to the HOR at the anode, and thus, it requires higher PGM utilization contributing significantly to the cost. 22 Consequently, lowering the electrocatalyst cost for the ORR is critical to accelerating the commercial application of PEMFCs. This is why a substantial effort has been devoted to rationally

Received: October 6, 2023
Revised: December 6, 2023
Accepted: December 11, 2023



designing low-cost electrocatalysts for ORR. Although recent successes in developing advanced Pt-metal (M) alloy electrocatalysts can further reduce Pt loading to 0.1 mg cm<sup>-2</sup> for ORR,<sup>23</sup> the intrinsic instability of base metals in Pt-M crystalline structures can lead to significant performance loss and high possible contamination to ionomer and membranes.<sup>24</sup> Additionally, a much higher Pt loading (0.3–0.4 mg cm<sup>-2</sup>) is required by the desirable heavy-duty fuel cell vehicles to counter the severe performance degradation during long-term applications (up to 25 000 h).<sup>25</sup> Therefore, the utmost goal is to develop PGM-free electrocatalysts with high activity, excellent stability, and low cost to accelerate future large-scale commercialization of PEMFCs.

Toward this goal, metal-nitrogen-doped carbon (M-N-C) electrocatalysts have been developed and have shown the most promising ORR activity and reasonable stability under the acidic environments desirable for PEMFCs. 15,26-29 The M component is usually referred to as Earth-abundant Fe or Co, and the atomically dispersed M moieties are coordinated with nitrogen atoms (e.g., Fe-N<sub>4</sub>) as the recognized most active sites toward ORR.<sup>21</sup> Especially, the most active Fe-N-C electrocatalyst, with a high mass loading of around 0.6 mg cm<sup>-2</sup>, has been close to the catalytic activity of Pt electrocatalysts at 0.06 mg cm<sup>-2</sup> under acidic medium in rotating disk electrode (RDE) tests.<sup>30</sup> Moreover, it has been demonstrated that the performance of the Fe-N-C electrocatalyst with a loading of about 4 mg cm<sup>-2</sup> in membrane electrode assembly (MEA) is comparable with that of the Pt electrocatalyst at a loading of 0.1 mg cm<sup>-2</sup>. <sup>31</sup> Nevertheless, the long-term durability of these highly active Fe-N-C electrocatalysts under the practical conditions of PEMFCs is still far from satisfactory. The performance degradation usually exceeds 50% after 100 h of measurement at a constant voltage of 0.6 V. 32,33 The poor durability of Fe-N-C electrocatalysts must be addressed before PGM-free cathode electrocatalysts can be applied for PEMFC applications. Thus, elucidation of degradation mechanisms of Fe-N-C electrocatalysts toward the ORR is a critical step to enhance the durability. To date, there are few suggested mechanisms of ORR promoted by the catalysts based on Earth-abundant metals, but the exact structure of a catalytic center and subsequent intermediates participating in 4-electron ORR still needs to be determined.34-3

Herein, we employed synchrotron-based X-ray spectroscopy, a powerful research tool in heterogeneous catalysis capable of establishing plausible catalytic mechanisms in ORR driven by these complex dynamic systems.<sup>36–43</sup> Detailed XANES and XES analyses of Fe-N-C electrocatalysts and their formulations with Nafion were presented recently.<sup>44</sup> Using an in situ electrochemical cell, we were able to characterize the reactive transformations of the known Fe-N-C electrocatalyst  $^{26}$  under applied potential in acidic (pH = 1) solutions. The X-ray absorption near-edge structure (XANES), the extended X-ray absorption fine structure (EXAFS), and X-ray emission spectroscopy (XES) were used to reveal the oxidation state and coordination environment of the as-prepared materials and reactive intermediates during electrocatalytic ORR. Surprisingly, the addition of Nafion, the most widely used ionomer, resulted in pronounced changes in the XAS spectra consistent with partial reduction of Fe centers to the Fe<sup>2+</sup> state, a decrease in the content of short Fe-Fe interactions, and an increase in the content of long Fe-Fe interactions at ~3.1 Å. Long Fe-Fe interactions at ~3.1 Å

were shown to be a feature of Fe<sup>3+</sup> ions bound with the Nafion, indicating a strong catalyst—ionomer interaction. While XES spectra and Nafion-induced changes in XANES are very similar to the data detailed in the earlier report,<sup>44</sup> unique EXAFS results allowed us to make novel inferences on the strong catalyst—ionomer interaction.

## 2. RESULTS AND DISCUSSION

**2.1. XAS Characterization of the Pristine Materials.** Figure 1 shows Fe K-edge XANES of the pristine (as prepared)

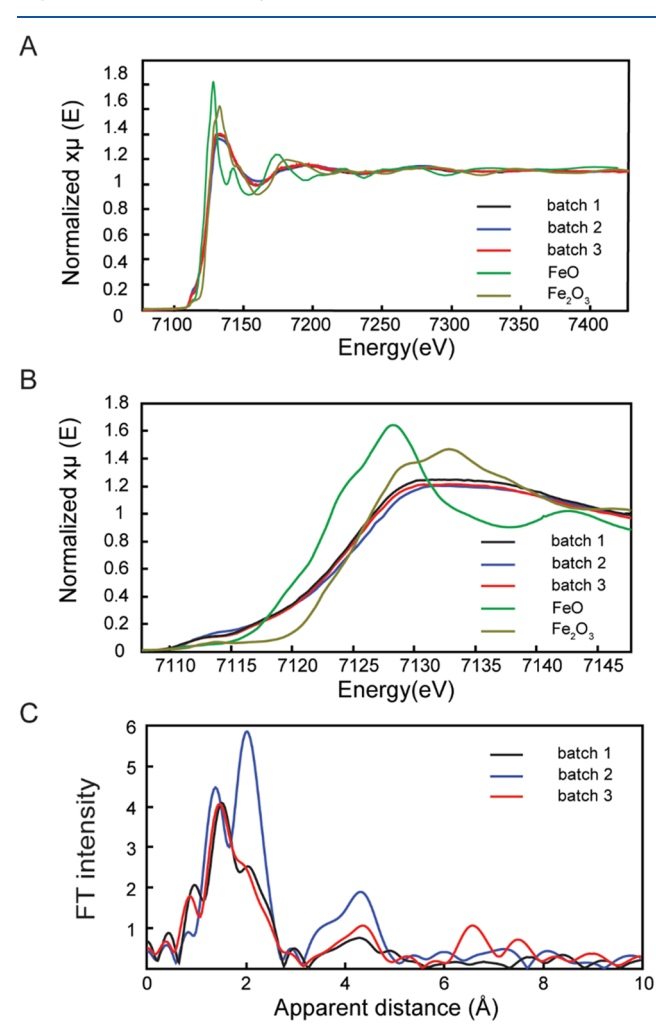


**Figure 1.** Fe K-edge of the as-prepared catalysts measured as pellets using an X-ray fluorescence signal: (A, B) XANES (in comparison with iron oxide standards FeO and  $Fe_2O_3$ ); (C) EXAFS of batch 1, 2, and 3 catalysts.

catalytic powders [product codes: 230–002-C29 (batch 1), 230–002-C30 (batch 2), 230–002-C31 (batch 3)] measured as pellets using an X-ray fluorescence signal. Different batches here designate the same catalyst prepared by the same procedures in three separate preparations. Thus, we expect minimal differences in composition and performance of these materials attributable only to minute differences in preparations. The comprehensive characterization and electrochemical evaluation of these materials were performed in the previously published work.<sup>26</sup> It was demonstrated that materials of batch 2 and batch 3 have a similar activity (in MEA tests) and outperform batch 1. Comparison of the Fe K-edge of catalysts

Table 1. Structural Parameters from EXAFS Fits for the As-Prepared Catalytic Powders

sample	fit #	shell	R, Å	N	$\sigma^2 \times 10^3$	R-factor	reduced Chi <sup>2</sup>
batch 1	1	Fe-N	2.00	4	9.5	0.23	39 648
powder	2	Fe-N	2.03	4	10.2	0.015	4953
k-space: 3.46-11.5 (Å <sup>-1</sup> )		Fe-Fe	2.56	1	9.4		
R-space: 1.22-2.65 (Å)	3	Fe-N	2.00	4	9.7	0.0013	429
		Fe-Fe	2.54	0.5	2.4		
	4	Fe-N	2.01	4	9.5	0.0	66
		Fe-Fe	2.54	0.4	0.9		
		Fe-C	3.25	2	29		
batch 2	1	Fe-N	2.04	4	8.6	0.46	80 542
powder	2	Fe-N	1.95	4	8.4	0.013	4272
k-space: $3.46-11.5(Å^{-1})$		Fe-Fe	2.49	1	1.2		
R-space: 1.08-2.60 (Å)	3	Fe-N	1.94	4	9.1	0.0009	295
		Fe-Fe	2.48	1.5	4.1		
batch 3	1	Fe-N	2.00	4	8.7	0.003	218
powder		Fe-Fe	2.52	0.4	0.6		
k-space: 3.46-11.5 (Å <sup>-1</sup> )	2	Fe-N	1.99	4	8.8	0.001	118
R-space: 1.22-2.65 (Å)		Fe-Fe	2.51	0.6	3.6		
		Fe-C	2.71	2	7.5		

<sup>&</sup>quot;Fits were done in q-space. R is the Fe-backscatter distance.  $\sigma^2$  is the Debye-Waller factor. R-factor and reduced Chi<sup>2</sup> are the goodness-of-fit parameters (see XAS/EXAFS Section in the text).  $S_0^2 = 1$  was used in all fits. The best fits are shown in Figure S1.

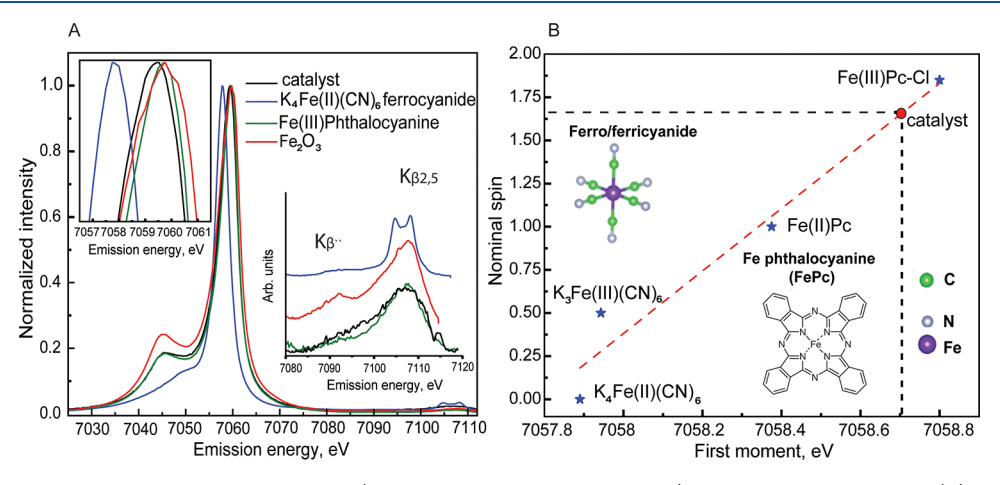


Figure 2. (A) Fe  $K_{\beta}$  XES spectra of the Fe-N-C catalyst (batches 1-3 gave the same results) and standard compounds; (B) correlation of the first moment and nominal spin.

and iron oxides (FeO and Fe2O3) also measured as pellets in transmission (to avoid effects of self-absorption) shows that catalysts have the majority Fe centers in the Fe3+ oxidation state (Figure 1A,B). XANES also shows pre-edge intensities in a broad range from 7110 eV to the rising edge above 7120 eV. The pre-edge feature at  $\sim$ 7113 eV reflects the 1s  $\rightarrow$  3d transition, while the pre-edge peak at ~7119 eV was earlier assigned to 1s  $\rightarrow$  4p<sub>z</sub> in Fe atoms embedded into Fe-N-C matrix of distorted phthalocyanine-like moieties.<sup>36</sup> It is known from earlier analysis 41 and confirmed below by EXAFS that catalyst samples contain some amounts of Fe metal nanoparticles and/or Fe-carbide species. Note the absorption edge of these formally Fe<sup>0</sup> species is at the lower energy ( $\sim$ 7113 eV) compared to Fe3+, and they can also contribute to spectral intensities in the pre-edge region. The increase in pre-edge intensity of XANES for batch 2 is well captured by a linear combination of spectra for the Fe metal (4.5%) and batch 1 (96.5%) (see Figure S3), signifying a higher content of Fe<sup>0</sup> nanoparticles such as Fe metal and/or Fe-carbide in batch 2.

EXAFS Fourier transforms (R-space) of three batches of the catalyst (Figure 1C) slightly differ from the analogues reported earlier. 37,38,41,42 The prominent peak at ~1.5 Å apparent distance corresponds to the first coordination sphere of Fe and is typical for Fe-N interactions.<sup>34</sup> The peak at apparent distance ~2.0 Å corresponds to Fe-Fe interaction in metallic Fe and Fe-carbide species, while Fe-C backscattering peaks of the Fe-N-C second coordination sphere are expected at ~2.5 A apparent distance and are characteristic for single site Fe species embedded in the C/N environment. Similar spectroscopic features for Fe metal, cementite (Fe<sub>3</sub>C) nanoparticles, and Fe inside the C/N pyrrolic matrix were reported earlier. 41,45,46 The peak at ~4.3 Å, particularly prominent in batch 2 of the catalyst, is likely a multiple scattering of Fe-Fe-Fe shells that may be attributed to the presence of trace amounts of Fe and Fe-carbide nanoparticles in the catalysts. 26,40 EXAFS fits in Table 1 and Figure S1 elaborate upon these tentative peak assignments and provide relevant distances.

Data for all three batches are satisfactory fit with four Fe-N absorber-backscatters at ~2.0 Å, some Fe-Fe at ~2.5 Å (Nnumber here varies from N = 0.4-0.6 for batch 1 and 3 catalysts to N = 1.5 for batch 2), and a few Fe-C at  $\sim 3.2$  Å in batch 1 and 3 catalysts (Table 1). The Fe-C coordination sphere appears to be highly disordered as evident from the high Debye-Waller factor for this shell. Combined XANES and EXAFS characterization shows that in batches 1 and 3, the majority of the iron sites represent mononuclear Fe centers outfitted, in agreement with the previous XPS and Mossbauer data, with the pyrrolic coordination environment of phthalocyanine type. 26,41,42 However, batch 2 exhibits a slight increase in XANES intensity at ~7114 eV and more prominent peaks in EXAFS at ~2.0 and ~4.3 Å apparent distances, corresponding to Fe-Fe interactions of metallic Fe or Fecarbide nanoparticles.<sup>26</sup> Therefore, while three batches of the catalyst have noticeable variability in the intensity of EXAFS peaks for short Fe-Fe (~2.0 Å apparent distance) interaction, in reality, they differ only by a small, (<5% content) of Fe and/ or Fe-carbide particles with formal Fe oxidation state Fe<sup>0</sup> (see Figure S3). Thus, EXAFS data reflect the highly heterogeneous nature of the aforementioned catalysts, 37,38 as well as the challenge in preparing the catalyst with exact Fe-N-C composition.

**2.2.** X-ray Emission Spectroscopy (XES) Characterization of the Pristine Materials. To characterize the spin and oxidation states of iron ions in the prepared catalysts, we employed X-ray emission spectroscopy. The capability of XES to quantify the spin state of a series of Fe–N–C catalysts was highlighted in previous studies. Figure 2A shows the XES for the catalyst and a set of Fe standards for which the nominal spin and oxidation state of iron ions are well-characterized (see Table 2). The XES of the catalyst features a  $K_{\beta 1,3}$  main line at

Table 2. Characteristics of Fe Complexes from Formal and Spectral Analysis

compound	spin state <sup>a</sup>	nominal spin
$Fe_2O_3$	HS	2.5
Fe <sup>3+</sup> (Pc)Cl	mix IS and HS	1.85 <sup>48,49</sup>
$Fe^{2+}(Pc)$	IS	1 <sup>53,54</sup>
K <sub>3</sub> Fe <sup>3+</sup> (CN) <sub>6</sub> ferricyanide	LS	$0.5^{55,56}$
K <sub>4</sub> Fe <sup>2+</sup> (CN) <sub>6</sub> ferrocyanide	LS	0 <sup>57</sup>
Fe-N-C	mix	1.66 <sup>b</sup>

<sup>a</sup>High spin (HS); low spin (LS); intermediate spin (IS). <sup>b</sup>Determined from spectral analysis; see Figure 2B.

7059.5 keV accompanied by a pronounced  $K_{\beta'}$  shoulder at 7045.4 keV. The shape of  $K_{\beta'}$ ,  $K_{\beta 1,3}$ , and crossover peaks measured for a catalyst resembles the one for Fe3+ phthalocyanine and Fe<sub>2</sub>O<sub>3</sub> (see Figure 2A, inset). Closer examination indicates that catalyst spectra feature a lesspronounced  $K_{\beta'}$  shoulder and the position of the  $K_{\beta 1,3}$  peak for the catalyst is shifted by ~0.3 eV toward lower energies compared to the one for Fe<sup>3+</sup> phthalocyanine and Fe<sub>2</sub>O<sub>3</sub>. The spectral variation of iron with nominal same spin and oxidation states can be associated with the influence of the surrounding atoms referred to as the covalency effects, 47 as well as due to a mixture of multiple species in the sample. The iron ion in Fe<sup>3+</sup> phthalocyanine is present in high spin (HS) (S = 5/2) and intermediate spin (IS) (3/2) configurations. 48,49 The similarity of the catalyst, Fe<sub>2</sub>O<sub>3</sub>, and Fe<sup>3+</sup> phthalocyanine spectra may imply that iron in the catalyst is present in the 3+ oxidation

state and has a predominantly high spin configuration. The Fe<sup>3+</sup> oxidation state assignment is in agreement with the XANES results above. To quantify the correlation between changes in the spin state and peak position, we calculated first moments FM =  $\sum_{i} (E_{i}I_{i})/\sum_{i}I_{i}$ , where  $E_{i}$  is the emission energy and Ii is the intensity of the spectrum at that energy. Analysis was done over the 7053-7065 eV range, which covers the Fe  $K_{\beta 1,3}$  spectral lines (see Figure 2B). First moments have been demonstrated to vary linearly with spin.<sup>47</sup> To compare with materials having similar ligands, the first-moment curve was generated by using a subset of model compounds with N or C atoms located in the first coordination of iron. The firstmoment analysis is particularly relevant for the study of species with unknown and/or complex spin states; for example, calculated values can be used to predict the spin of iron in Fe-N-C, lacking the detailed ligand-field structure and ligandorbit coupling of their  $Fe-N_x$  sites.

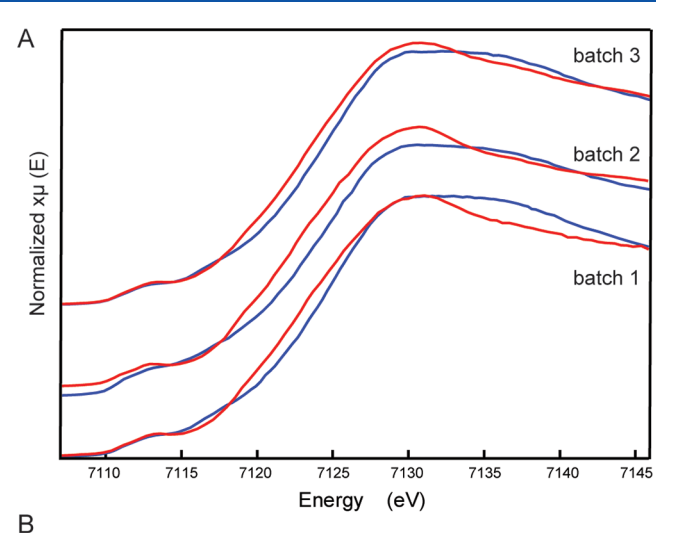
The FM analysis results in spin 1.66, corresponding to the calculated value of the first moment, which is close to the 1.85 observed for the Fe<sup>3+</sup> phthalocyanine—itself exceeding twice the value of 0.8 reported for Fe-N-C material in ref 38 (note that ref 38 used a different type of analysis based on the fitting  $K_{\beta}$  line). We attribute this difference to a significantly higher content of single site Fe<sup>3+</sup>-N<sub>x</sub> centers in these Fe-N-C preparations and significantly lower content of Fe<sup>0</sup> and Fecarbide nanoparticles for which lower spin values are expected. The linear fit of integrated absolute differences (IAD) values presented in later work by Saveleva et al. 44 results in value ~1.9 for pristine Fe-N-C powder, close to the one obtained here. Aiming to analyze crossover satellites, our iron spectrometer was designed to cover the spectral range up to 7120 eV. 50 The  $K_{\beta''}$  and  $K_{\beta 2,5}$  satellite lines of catalyst and iron compounds with oxygen, nitrogen, and carbon atoms in the first coordination sphere of iron are shown in the inset of Figure 2A. Spectra over the 7080-7120 eV energy range were corrected for background using polynomial fit through baseline points outside the area with signal and were plotted on an arbitrary intensity scale to facilitate comparisons. The obtained spectra are consistent with the ones reported in the literature for Fe<sub>2</sub>O<sub>3</sub>, 51 solution-phase ferrocyanide, 52 and pristine catalyst powder.44

The  $K_{\beta 2.5}$  transitions directly below the Fermi level are clearly seen for studied compounds. The  $K_{\beta''}$  or "crossover" peak at lower fluorescence (or higher binding) energies in transition metal complexes is assigned to ligand 2s to metal 1s crossover transitions<sup>58</sup> and is most intense for Fe<sub>2</sub>O<sub>3</sub> and Fe<sup>2+</sup> ferrocyanide. The relative shifts between the crossover fluorescence energies for different ligands correspond mainly to the shifts in 2s binding energies of the atomic species by approximately the ligand 2s binding energies, while the crossover intensity varies with metal-ligand distance. The  $K_{\theta''}$  for  $Fe^{2+}$  ferrocyanide and  $Fe_2O_3$  peaks are the most pronounced, which is consistent with the similar metal-ligand bond length of ~1.9 Å for Fe-O and Fe-C in these compounds. The Fe-N distance in Fe-N/C catalysts is longer [~2.0 Å determined by EXAFS (Table 1)], which results in lower intensity of the  $K_{\beta''}$  crossover peak, Figure 2A, inset. Earlier studies also indicated a low intensity of this spectral feature.44 Overall, the catalyst spectrum matches most of Fephthalocyanine features (Figure 2A, insert) in the  $K_{\beta 2.5}$  region but also has some additional intensities, likely due to the presence of additional species.

2.3. XAS Characterization of the Electrocatalytic Layer Formed from the Catalyst and Nafion. The electrocatalytic layer was prepared on the grafoil electrode by dropcasting the catalytic ink prepared from 2 mg of the catalyst (Materials and Methods). We tested ink preparation with sonication and without, and no differences were noted on the resulting XAS spectra. After drying for 24 h, the electrodes were subjected to XAS study, first as it is (dry) and later, in the presence of an electrolyte (0.1 M HClO<sub>4</sub>) inside the *in situ* cell. As no differences between these two cases (in dry or hydrated form) were noted, we discussed these measurements together without noting the difference between the two (same for the ink preparation with or without sonication). In the control experiment, which excluded the catalyst material, the Nafion alone was deposited on the grafoil, and the absence of Fe signal was confirmed, indicating no Fe contamination in the used grafoil, Nafion, and solvents (data not shown). The addition of the ionomer (5 wt % Nafion solution in ethanol) to the catalyst leads to changes in XANES (Figure 3A). For all three batches of the catalysts, we observed a decrease in the pre-edge intensity at ~7117 eV, a ~0.7 eV edge shift to lower energy, and a decrease in the postedge intensity above 7135 eV. These combined changes indicate the admixture of some Fe<sup>2+</sup> species, as well as changes in the ligand environment of iron ions. Although the pre-edge feature at ~7113 eV corresponding to  $1s \rightarrow 3d$  transition remains unchanged after ionomer addition, a decrease in the pre-edge peak ( $\sim$ 7117 eV, 1s  $\rightarrow$  4p) may signify a modification of the ligand environment. Visually, overall changes in the XANES are very similar to those reported earlier<sup>44</sup> for samples with added Nafion, while another study reported no change in XANES, but EXAFS was visually different. 43 When a change is observed, the initially flat top of the XANES (7130-7135 eV range) gains a pointy shape at ~7129 eV. Such changes in the white line intensity are consistent with the increase in the coordination number of Fe centers potentially resulting from additional oxygen ligands.<sup>59</sup> In addition, the earlier work<sup>44</sup> reported XANES shift to higher energy while we observed the opposite, Figure 3A.

We can speculate that the initial Fe3+ composition of the sample with a small admixture of Fe<sup>0</sup> species has evolved to have some Fe<sup>2+</sup> character (Figure 3A), possibly via the reduction of Fe<sup>3+</sup> by Fe<sup>0</sup> species in the presence of ionomer. While changes in XANES suggested possible structural rearrangements of the Fe environment, Fourier-transformed EXAFS directly confirmed it (Figure 3B). After Nafion addition, a prominent new peak appears at an apparent distance of ~2.5 Å, reflecting deep restructuring of the catalyst. The only other study reporting the EXAFS before and after formulation with Nafion did not analyze EXAFS in detail despite visual differences in the Fourier-transformed spectra. 43 This could be due to insufficient EXAFS data quality. We do not think that observed changes in EXAFS are due to other factors such as solvent or air exposure; catalyst samples were acid leached multiple times as a part of the catalyst preparation protocol, already undergoing solvent/acid exposure. Samples were also kept open to the air after preparation. Thus, any effect of electrolyte exposure and oxygen exposure should already manifest when the initial powders were analyzed by XAS.

To test the hypothesis of the role of Nafion in catalyst restructuring, we measured EXAFS of Nafion spiked with a trace amount of  $Fe^{3+}$  salt solution (Figure 3B). We indeed reproduced the formation of a new peak around  $\sim 2.5$  Å



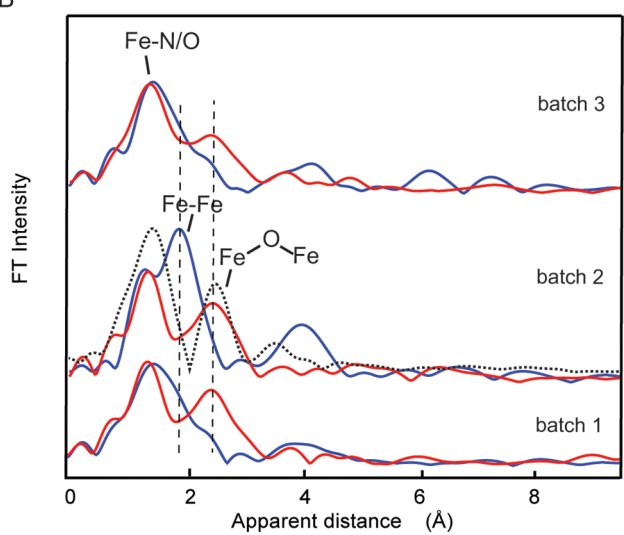


**Figure 3.** XANES (A) and EXAFS (B) characterization of the electrocatalytic layer formed from the catalyst and Nafion. Comparison of batch 1, 2, and 3 catalysts before (blue) and after (red) Nafion addition with the overlaid control sample of  ${\rm Fe}^{3+}$  in Nafion on grafoil (B, dashed line). Electrocatalytic layers of different batches were characterized as dry and later in the presence of an electrolyte (0.1 M HClO<sub>4</sub>) inside the *in situ* cell with no differences noted.

apparent distance (Figure 3B), which we tentatively assigned to the engagement of oxygen atoms of the ionomer in Fe coordination resulting in the formation of Fe-O-Fe moieties, such as  $\mu$ -oxo-bridges.<sup>36</sup> Earlier studies suggested the formation of Fe-dimers and trimers in Nafion. 60 Results of EXAFS fits are given in Tables 3 and S1 and in Figure S2. They show that the main peaks are due to Fe-O interaction at ~2.0 Å and Fe-O-Fe bridge with Fe-Fe distance at ~3.1 Å, in agreement with the proposed  $\mu$ -oxo-bridge structure. Although detailed X-ray photoelectron spectroscopy (XPS), scanning transmission electron microscopy (STEM), and X-ray spectroscopic characterizations of similar materials after addition of Nafion ionomer were reported previously, 36,44 no EXAFS characterization of the ORR catalyst-ionomer composite uncovered similar effect to the one reported here. We combined EXAFS data for all three batches of catalyst mixed with Nafion due to the low difference in data obtained from batches 1-3, see Figure 3B. Fits for catalyst mixed with Nafion are given in Tables 3 and S2 and Figure S2. Here, the

Table 3. Structural Parameters from EXAFS Fits<sup>a</sup> for the Fe<sup>3+</sup>-Spiked Nafion and Catalytic Powder after the Addition of Nafion

sample	fit <sup>b</sup> #	shell	R, Å	N	$\sigma^2 \times 10^3$	R-factor	reduced Chi <sup>2</sup>
Fe <sup>3+</sup> -spiked Nafion	Table S1 fit# 5	Fe-O	1.98	4	11.0*	0.0019	712
$k$ -space: 3.54–10.0 ( $\mathring{A}^{-1}$ )		Fe-O	2.23	2	11.0*		
R-space: 1.08-3.2 (Å)		Fe-O	2.52	1	1.0		
		Fe-Fe	3.08	1	3.5		
catalytic powder after addition of Nafion k-space: 3.54-10.0 ( $\mathring{A}^{-1}$ )	Table S2 fit# 5	Fe-O	1.98	2	3.7	0.001	1081
		Fe-N	2.22	2	23.0		
		Fe-Fe	2.59	0.2	6.0		
R-space: 1.02-3.4 (Å)		Fe-Fe	3.12	1	3.4		

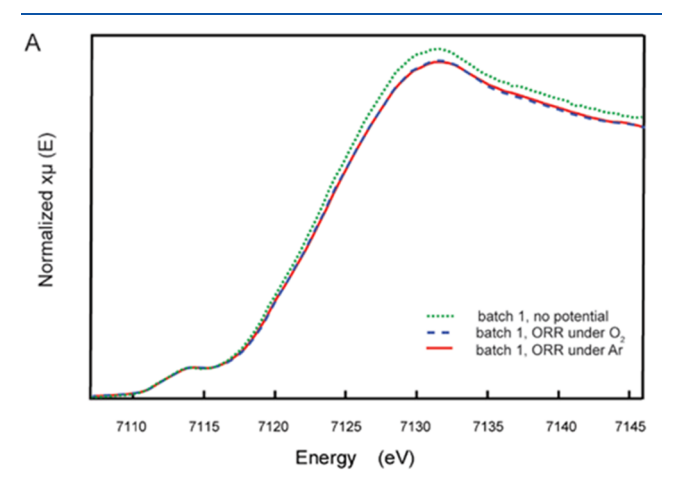
<sup>&</sup>lt;sup>a</sup>Fits were done in q-space. R is the Fe-backscatter distance.  $σ^2$  is the Debye-Waller factor. R-factor and reduced Chi² are the goodness-of-fit parameters (see XAS/EXAFS Section in the text).  $S_0^2 = 1$  was used in all fits. \*Same parameter is used with multiple shells. <sup>b</sup>More fits are given in Tables S1 and S2.

first coordination sphere of Fe can be fitted with a combination of Fe-O and Fe-N absorber-backscatter distances, Tables 3 and S2. Most prominent higher coordination spheres are due to Fe-Fe interactions at ~2.6 and ~3.1 Å. While the Fe-Fe interaction at  $\sim$ 2.6 Å is likely the same as that in the starting catalyst, Fe-Fe at ~3.1 Å appears after the addition of Nafion. Thus, the appearance of ~3.1 Å distance for catalysts (Figure 3B) may result from the partial removal of Fe embedded in the N-C matrix by chelation to Nafion with the formation of multinuclear Fe centers. This may reflect the initial as-prepared catalyst having edged catalytic metal centers sterically accessible toward chelation with Nafion ionomer rather than located inside a basal plane of graphitic-layered material.<sup>61</sup> Theoretical DFT calculations highlighted partial demetalation of PGM-free catalysts as the main mechanism of catalyst deactivation.<sup>62</sup> Per reviewer suggestion, we expanded the study of interaction of Fe-N-C with Nafion to Fe-phthalocyanine (FePc) interaction with Nafion to determine how specific or general the interaction of the Fe-N<sub>4</sub> fragment with Nafion might be. For this, we performed ultraviolet-visible (UV-vis) absorption measurements and EXAFS for solutions of FePc in dimethylformamide (DMF) with and without Nafion (Figure S4). Indeed, the addition of Nafion to the initial solutions of different concentrations results in UV-vis spectra similar to the metal-free phthalocyanine, Figure S4A.63 Fe3+-spiked Nafion and FePc in dimethylformamide prepared with Nafion and dropcast on grafoil show similar EXAFS peaks; both spectra differ from that of initial FePc, Figure S4B. This result indicates the potential release of metal ions from FePc in the presence of Nafion.

It should be mentioned that despite acid treatment of Fe-N-C catalysts in order to remove pore formers and unreacted iron particles, some particles remain protected by graphene layers. Based on our previous observations, the number of graphene layers in PGM-free materials is between 10–20, <sup>28</sup> and the energy of an ultrasonic probe can expand these layers, exposing metallic iron particles to strong acidic ionomer, <sup>64</sup> followed by partial dissolution of Fe nanoparticles.

**2.4.** *In Situ* XAS Characterization of the Electrocatalytic Layer. Grafoil electrodes with the catalytic ink prepared by mixing the catalyst and Nafion were mounted in the custom-made electrochemical cell as a wall on the X-ray beam path with a catalyst layer facing into the cell (Figure S5). Other electrodes were platinum wire as a counter electrode and Ag/AgCl as a reference electrode. All *in situ* measurements were done with the cell filled with 0.1 M HClO<sub>4</sub>, and oxygen or argon was bubbled during the measurements under a +0.1 V

vs Ag/AgCl applied potential. All batches behaved the same in terms of Fe K-edge XANES and EXAFS, and no significant spectral differences were noted when the potential was applied. The lack of considerable changes confirms the stabilization of Fe catalytic centers by the Nafion ionomer and the overall stability and robustness of the catalyst during prolonged ORR. No visible changes in XAS spectra were noted for the catalyst in oxygen- or argon-saturated electrolyte supported by continuous gas bubbling under an applied potential of +0.1 V vs Ag/AgCl (Figure 4). The lack of spectral changes in the



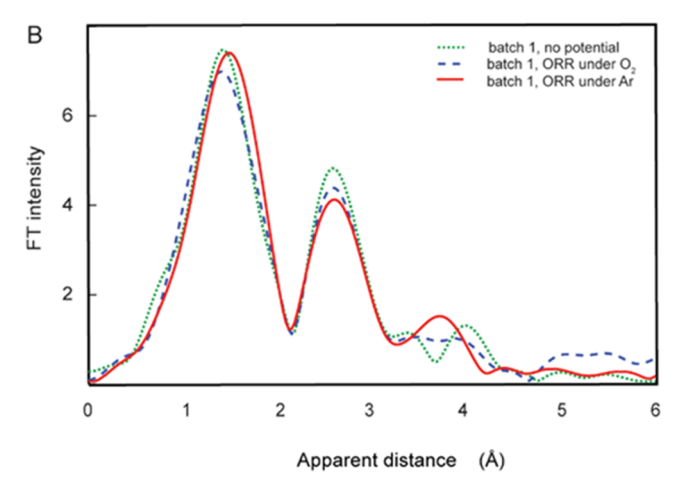


Figure 4. Comparison of XANES (A) and EXAFS (B) of electrocatalytic layers for the Fe–N–C batch 1 catalyst under ORR conditions (+0.1 V vs Ag/AgCl in 0.1 M  $HClO_4$ ) under  $O_2$  and Ar.

presence or absence of oxygen is in agreement with earlier observations by Jia et al.<sup>34</sup> Inordinately, Jia et al.<sup>34</sup> did not analyze coordination spheres beyond the Fe-N first coordination. We consider the presence of Nafion to be essential, as it is used in a real fuel cell. We have not tried to measure the system under a more positive potential. We expected that in agreement with earlier studies, 34,37,38 we might observe the oxidation of Fe centers and increased Fe<sup>3+</sup> content at higher potentials. However we attempted to see a reactive intermediate, and thus, we tried for the highest content of Fe<sup>2+</sup> centers that should be active in binding oxygen. Here, we conclude that the current sample, despite being highly active and containing large numbers of Fe-N<sub>4</sub> single-cite centers, is still not suitable for detection of the reactive intermediates, likely due to interference of Fe bound to Nafion, which is not catalytically active. One study detected the release of Fe ions from the Fe-N-C/Nafion-based fuel cell cathode under the condition of the acerated durability test. 43 Such release is potentially possible from the catalyst itself as well as from Fe binding sites in Nafion.

In conclusion, X-ray absorption at Fe K-edge and Fe  $K_{\beta}$  X-ray emission (XES) spectroscopies were used to study the electronic structure of Fe centers in the highly active Fe–N–C oxygen reduction catalyst and in its formulation with Nafion for use in a PEM fuel cell. Spectroscopic probes have shown a large content of Fe–N $_x$  centers. The observed formation of Fe–O–Fe groups, associated with reduction of Fe–Fe bond peak intensity when the Fe–N–C material is mixed with Nafion containing ink, can be associated with interaction of iron nanoparticles and Fe-N $_4$  centers with –SO $_3$ H groups from the ionomer.

## 3. CONCLUSIONS

Combined Fe K-edge XANES and Fe  $K_{\beta}$  XES analyses have shown that highly active Fe-N-C ORR catalysts contain Fe<sup>3+</sup> high spin centers as majority species (~95%). These centers have a single site Fe with nitrogen coordination. The largest spectral changes happen when these catalysts are formulated with Nafion where XANES shape changes in a similar way as previously reported and might reflect the coordination sphere expansion from 4-5-coordinate Fe to 6-coordinate Fe. Strikingly, EXAFS changes are consistent with Fe<sup>3+</sup> ions migrating into the Nafion with the appearance of long Fe-Fe interaction at ~3.1 Å, which is absent in the initial catalyst, and were shown to be a feature of Fe<sup>3+</sup> ions bound with the Nafion in the control experiment. Fe<sup>3+</sup> ions bound with the Nafion are inactive in ORR. Thus, our experiment shows that interaction of the Fe-N-C system with Nafion is different from the aggressive acid leaching and might extract Fe3+ ions, which otherwise survive intense acid leaching. This observation has a consequence for catalyst design as the question arises whether only Fe single site centers inaccessible to Nafion or too strongly bound to the N-C matrix to be extracted by Nafion are true catalytic sites. Other possible source of Fe<sup>3+</sup> bound to Nafion can be Fe metal nanoparticles in the case if Nafion is capable of disrupting protecting graphene layers. However, per sample composition, the Fe content in nanoparticle form is rather low and does not exceed ~5% of the total Fe in Fe-N-C catalysts analyzed here. Thus, for Fe-N-C ORR catalysts, analysis of Fe speciation in both as-prepared Fe-N-C and ink formulations should be recommended to uncover the true distribution of ORR active centers.

#### 4. MATERIALS AND METHODS

The catalyst was obtained from Pajarito Powder, LLC (Albuquerque, NM). Product codes: 230–002-C29 (batch 1), 230–002-C30 (batch 2), and 230–002-C31 (batch 3) designate the same catalyst prepared by the same procedures in three separate preparations. 65,66 Additional references on the preparation procedure are presented in the Supporting Information.

All chemicals and solvents were purchased from Sigma-Aldrich. Aqueous solutions were prepared using ultrapure (Type 1) water (resistivity 18.2 M $\Omega$ ·cm at 250C) from a Q-POD unit of a Milli-Q integral water purification system (Millipore, Billerica, MA).

Catalytic ink was prepared from 2 mg of the catalyst sonicated with 4  $\mu$ L of 5% Nafion solution in ethanol (Sigma-Aldrich) diluted into 0.25 mL of isopropanol for 15 min followed by dropcasting on 1 cm² of grafoil. GraFoil material is graphite foil made from graphite flakes. After drying for 24 h, the electrodes were subjected to XAS study first as it is (dry) followed by addition of an electrolyte (0.1 M HClO<sub>4</sub>). A Fe³+-containing Nafion layer on the grafoil surface was prepared as follows. 0.1 mg of Fe(NO<sub>3</sub>) $_3$ ·9H<sub>2</sub>O was dissolved in 0.1 mL of DI water followed by addition of 0.4 mL of ethanol and 8  $\mu$ L of Nafion. The obtained mixture was dropcast on a 2 cm² grafoil electrode and dried overnight.

For the UV–vis study, we prepared the 0.01, 0.02, 0.03, 0.04, and 0.05 mM solutions of Fe(II)Pc (Fisher Scientific, CAS 132-16-1) in dimethylformamide (DMF) followed by the addition of 1.6% v/v Nafion.

**4.1. Electrochemistry.** ORR catalysis experiments were accomplished using a potentiostat (CHI 627C; CH Instruments Inc., Austin, TX) using a standard single-compartment 3-electrode cell. The grafoil electrodes with the catalytic ink were electrically contacted using copper conductive tape and masked to a geometrical surface area of 1 cm². A piece of a platinum wire served as the counter electrode, and a saturated Ag/AgCl electrode served as the reference electrode. All reported measurements were repeated three times to ensure the reproducibility of results. The cyclic voltammetry (CV) data were collected continuously; based on the reproducibility of data for three repeated experiments, the error can be estimated on the level of 10%.

**4.2. X-ray Absorption Spectroscopy.** X-ray absorption spectra were collected at the Advanced Photon Source (APS) at Argonne National Laboratory at beamline 20-BM. The radiation was monochromatized by a Si(111) crystal. The intensity of the X-rays was monitored by three ion chambers:  $I_0$  filled with He/N<sub>2</sub> in a 2:3 ratio and  $I_1$  and  $I_2$  filled with 100% nitrogen. Iron metal foil was placed between  $I_2$  and  $I_3$ , and its absorption was recorded with each scan for energy calibration. The energy of the first derivative peak of the Fe metal foil was calibrated to a Fe K-edge energy of 7110.0 eV. The Fe X-ray fluorescence data were collected using an X-ray fluorescence detector. EXAFS scans with 10 eV steps in the pre-edge region (6980–6995 eV), 0.5 eV steps (6995–7260 eV) through the edge, and 0.05 Å  $^{-1}$  steps from k = 2.0-12 Å  $^{-1}$  were used.

**4.3. EXAFS Data Analysis.** Athena software was used for data processing. Energy scale for each scan was normalized using potassium permanganate powder standard, and scans for the same samples were added. Data in energy space were pre-edge corrected and normalized and background corrected. The processed data were converted to the photoelectron wave vector (k) space and weighted by  $k^3$ . The electron wavenumber is defined as in eq  $1^{68}$ 

$$k = (2m(E - E_0)/\hbar^2)^{1/2}$$
(1)

where  $E_0$  is the threshold energy. k-space data were truncated near zero crossings and Fourier-transformed into R-space. Artemis software was used for curve fitting. In order to fit the data, the Fourier peaks were isolated separately, or the entire experimental spectrum was fitted. The individual Fourier peaks were isolated by applying a Hanning window. Curve fitting was performed using ab initiocalculated phases and amplitudes from the FEFF8 program from the University of Washington. Ab initio-calculated phases and amplitudes were used in the EXAFS eq (eq 2)

$$\chi(k) = S_0^2 \sum_{i} \frac{N_j}{kR_j^2} f_{\text{eff}_j}(\pi, k, R_j) e^{-2\sigma_j^2 k^2} e^{-2R_j/\lambda_j(k)}$$

$$\sin(2kR_j + \varphi_{ij}(k))$$
(2)

where  $N_j$  is the number of atoms in the jth shell;  $R_j$  is the distance between the absorbing atoms and the atoms in the jth shell;  $f_{\rm effj}$  is the ab initio amplitude function for j, and  $e^{-2\sigma_j^2k^2}$  is the Debye–Waller factor for shell j accounting for damping due to thermal and static disorder in the shell. The mean free path term  $(e^{-2R_j/\lambda_j(k)})$  accounts for losses due to inelastic scattering. The oscillations in the EXAFS spectrum are reflected in the  $\sin(2kR_j+\varphi_{ij}(k))$  term, where  $\varphi_{ij}(k)$  is the ab initio phase function for the shell j.  $S_0$  is an amplitude reduction factor. The EXAFS equation was used to fit experimental data using N,  $E_0$ , R, and  $\sigma_2$  as variable parameters, while  $S_0$  was kept fixed. The quality of fit was evaluated by the R-factor: if the R-factor is less than 2%, then the fit is good enough. Reduced  $\chi^2$  was used to justify the addition of new absorber—backscatter shells.

4.4. X-ray Emission Spectroscopy.  $K_{\beta}$  XES spectroscopic measurements of the Fe-N-C oxygen reduction catalyst were conducted at the Inner Shell Spectroscopy (ISS) beamline (8-ID)<sup>69</sup> at the National Synchrotron Light Source II (NSLS-II) at Brookhaven National Laboratory. The NSLS-II storage ring operates at an electron energy of 3 GeV and a current of 400 mA. A Si(111) double-crystal monochromator was used. The incident beam absolute energy calibration was performed using a Fe foil by setting the first inflection point of the Fe K-edge to 7112 eV. The beam with a photon flux of  $\sim 10^{13}$  photons/s was focused to a beam size of 100  $\mu$ m  $\times$  100  $\mu$ m on the sample. The spectra were recorded using crystal Bragg analyzers reflecting the X-ray fluorescence onto an area detector (Dectris Pilatus 100 K). The design and characteristics of the spectrometer used are reported in previous studies. 50,70 The XES spectra were collected at an incident energy of 7.4 keV. Comparison of the XES spectra recorded with 1 and 200 s acquisition time did not show any radiation damage; thus, we rastered the sample on a 100  $\mu$ m  $\times$  100  $\mu$ m grid, acquiring XES spectra for 200 s at each spot.

# ASSOCIATED CONTENT

# **Solution** Supporting Information

The Supporting Information is available free of charge at https://pubs.acs.org/doi/10.1021/acsaem.3c02522.

Tables S1 and S2 and Figures S1 and S2: EXAFS fits of experimental EXAFS data, modeling of XANES data, UV—vis spectra for FePc in DMF with/without Nafion, characterization of Fe—N—C catalyst data, photograph of the experimental setup, details on sample preparations (PDF)

# AUTHOR INFORMATION

## **Corresponding Author**

Yulia Pushkar — Department of Physics, Purdue University, West Lafayette, Indiana 47907, United States; oorcid.org/0000-0001-7949-6472; Email: ypushkar@purdue.edu

#### **Authors**

Roman Ezhov — Department of Physics, Purdue University, West Lafayette, Indiana 47907, United States; orcid.org/ 0000-0001-6806-4033

Olga Maximova — Department of Physics, Purdue University, West Lafayette, Indiana 47907, United States; orcid.org/0000-0001-7789-6683

Xiang Lyu — Electrification and Energy Infrastructures Division, Oak Ridge National Laboratory, Oak Ridge, Tennessee 37831, United States; orcid.org/0000-0002-0867-3248 Denis Leshchev — National Synchrotron Light Source II NSLS-II, Brookhaven National Laboratory, Upton, New York 11973, United States; orcid.org/0000-0002-8049-

Eli Stavitski – National Synchrotron Light Source II NSLS-II, Brookhaven National Laboratory, Upton, New York 11973, United States

Alexey Serov — Electrification and Energy Infrastructures Division, Oak Ridge National Laboratory, Oak Ridge, Tennessee 37831, United States

Complete contact information is available at: https://pubs.acs.org/10.1021/acsaem.3c02522

#### **Author Contributions**

The manuscript was written through contributions of all authors.

#### **Notes**

The authors declare no competing financial interest.

## ACKNOWLEDGMENTS

This research was supported by NSF, CHE-2155060 (Y.P.) and by the US DOE Office of Energy Efficiency and Renewable Energy, Hydrogen and Fuel Cell Technologies Office, under the ElectroCat Consortium, DOE technology managers D. Peterson and D. Papageorgopoulos. The use of the Advanced Photon Source, an Office of Science User Facility operated by the US Department of Energy (DOE) Office of Science by Argonne National Laboratory, was supported by the US DOE under Contract DE-AC02-06CH11357. The PNC/XSD (Sector 20) facilities at the Advanced Photon Source and research at these facilities were supported by the US Department of Energy, Basic Energy Science and the Canadian Light Source. This research used beamline 8-ID (ISS) of the National Synchrotron Light Source II, a US Department of Energy (DOE) Office of Science User Facility operated for the DOE Office of Science by Brookhaven National Laboratory under Contract No. DE-SC0012704. This manuscript has been authored in part by UT-Battelle, LLC, under contract DE-AC05-00OR22725 with the US Department of Energy (DOE). The publisher, by accepting the article for publication, acknowledges that the US government retains a nonexclusive, paid-up, irrevocable, worldwide license to publish or reproduce the published form of this manuscript, or allow others to do so, for US government purposes. DOE will provide public access to these results of federally sponsored research in accordance with the DOE Public Access Plan (http://energy.gov/downloads/doe-public-access-plan). All authors acknowledge samples of Fe-N-C catalysts from Pajarito Powder, LLC.

# REFERENCES

- (1) Barkholtz, H. M.; Liu, D.-J. Advancements in rationally designed PGM-free fuel cell catalysts derived from metal—organic frameworks. *Mater. Horiz.* **2017**, *4* (1), 20–37.
- (2) Lyu, X.; Li, J.; Jafta, C. J.; Bai, Y.; Canales, C. P.; Magnus, F.; Ingason, Á. S.; Serov, A. Investigation of oxygen evolution reaction with Ni foam and stainless-steel mesh electrodes in alkaline seawater electrolysis. *J. Environ. Chem. Eng.* **2022**, *10* (5), No. 108486.
- (3) Qureshi, F.; Yusuf, M.; Kamyab, H.; Vo, D.-V. N.; Chelliapan, S.; Joo, S.-W.; Vasseghian, Y. Latest eco-friendly avenues on hydrogen production towards a circular bioeconomy: Currents challenges, innovative insights, and future perspectives. *Renewable Sustainable Energy Rev.* 2022, 168, No. 112916.

- (4) Zhiznin, S. Z.; Timokhov, V. M.; Gusev, A. L. Economic aspects of nuclear and hydrogen energy in the world and Russia. *Int. J. Hydrogen Energy* **2020**, 45 (56), 31353–31366.
- (5) Tanç, B.; Arat, H. T.; Conker, Ç.; Baltacioğlu, E.; Aydin, K. Energy distribution analyses of an additional traction battery on hydrogen fuel cell hybrid electric vehicle. *Int. J. Hydrogen Energy* **2020**, 45 (49), 26344–26356.
- (6) Pareek, A.; Dom, R.; Gupta, J.; Chandran, J.; Adepu, V.; Borse, P. H. Insights into renewable hydrogen energy: Recent advances and prospects. *Mater. Sci. Energy Technol.* **2020**, *3*, 319–327.
- (7) Hassan, N. S.; Jalil, A. A.; Khusnun, N. F.; Ahmad, A.; Abdullah, T. A. T.; Kasmani, R. M.; Norazahar, N.; Kamaroddin, M. F. A.; Vo, D. V. N. Photoelectrochemical water splitting using post-transition metal oxides for hydrogen production: a review. *Environ. Chem. Lett.* **2022**, 20 (1), 311–333.
- (8) Nicita, A.; Maggio, G.; Andaloro, A. P. F.; Squadrito, G. Green hydrogen as feedstock: Financial analysis of a photovoltaic-powered electrolysis plant. *Int. J. Hydrogen Energy* **2020**, 45 (20), 11395—11408.
- (9) Ishaq, H.; Dincer, I.; Crawford, C. A review on hydrogen production and utilization: Challenges and opportunities. *Int. J. Hydrogen Energy* **2022**, 47 (62), 26238–26264.
- (10) Foo, W. H.; Chia, W. Y.; Tang, D. Y. Y.; Koay, S. S. N.; Lim, S. S.; Chew, K. W. The conundrum of waste cooking oil: Transforming hazard into energy. *J. Hazard. Mater.* **2021**, *417*, No. 126129.
- (11) Zhang, B.; Sun, L. Artificial photosynthesis: opportunities and challenges of molecular catalysts. *Chem. Soc. Rev.* **2019**, 48 (7), 2216–2264
- (12) Ezhov, R.; Ravari, A. K.; Palenik, M.; Loomis, A.; Meira, D. M.; Savikhin, S.; Pushkar, Y. Photoexcitation of Fe3O nodes in MOF drives water oxidation at pH= 1 when Ru catalyst is present. *ChemSusChem* **2023**, *16* (5), No. e202202124, DOI: 10.1002/cssc.202202124.
- (13) Malik, V.; Srivastava, S.; Bhatnagar, M. K.; Vishnoi, M. Comparative study and analysis between Solid Oxide Fuel Cells (SOFC) and Proton Exchange Membrane (PEM) fuel cell A review. *Mater. Today: Proc.* **2021**, *47*, 2270–2275.
- (14) Barelli, L.; Bidini, G.; Gallorini, F.; Ottaviano, A. An energetic–exergetic comparison between PEMFC and SOFC-based micro-CHP systems. *Int. J. Hydrogen Energy* **2011**, *36* (4), 3206–3214.
- (15) Reshetenko, T.; Odgaard, M.; Randolf, G.; Ohtaki, K. K.; Bradley, J. P.; Zulevi, B.; Lyu, X.; Cullen, D. A.; Jafta, C. J.; Serov, A. Design of PGM-free cathodic catalyst layers for advanced PEM fuel cells. *Appl. Catal., B* **2022**, *312*, No. 121424, DOI: 10.1016/j.apcatb.2022.121424.
- (16) Yang, C.; Han, N.; Wang, Y.; Yuan, X.-Z.; Xu, J.; Huang, H.; Fan, J.; Li, H.; Wang, H. A Novel Approach to Fabricate Membrane Electrode Assembly by Directly Coating the Nafion Ionomer on Catalyst Layers for Proton-Exchange Membrane Fuel Cells. ACS Sustainable Chem. Eng. 2020, 8 (26), 9803–9812.
- (17) Firouzjaie, H. A.; Mustain, W. E. Catalytic Advantages, Challenges, and Priorities in Alkaline Membrane Fuel Cells. *ACS Catal.* **2020**, *10* (1), 225–234.
- (18) Gao, P.; Xie, Z.; Wu, X.; Ouyang, C.; Lei, T.; Yang, P.; Liu, C.; Wang, J.; Ouyang, T.; Huang, Q. Development of Ti bipolar plates with carbon/PTFE/TiN composites coating for PEMFCs. *Int. J. Hydrogen Energy* **2018**, 43 (45), 20947–20958.
- (19) Sarwar, M.; Gavartin, J. L.; Bonastre, A. M.; Lopez, S. G.; Thompsett, D.; Ball, S. C.; Krzystala, A.; Goldbeck, G.; French, S. A. Exploring fuel cell cathode materials using ab initio high throughput calculations and validation using carbon supported Pt alloy catalysts. *Phys. Chem. Chem. Phys.* **2020**, 22 (10), 5902–5914, DOI: 10.1039/d0cp00301h.
- (20) Guo, Y.; Pan, F.; Chen, W.; Ding, Z.; Yang, D.; Li, B.; Ming, P.; Zhang, C. The Controllable Design of Catalyst Inks to Enhance PEMFC Performance: A Review. *Electrochem. Energy Rev.* **2021**, *4* (1), 67–100.
- (21) Chung, H. T.; Cullen, D. A.; Higgins, D.; Sneed, B. T.; Holby, E. F.; More, K. L.; Zelenay, P. Direct atomic-level insight into the

- active sites of a high-performance PGM-free ORR catalyst. *Science* **2017**, 357 (6350), 479–484.
- (22) Debe, M. K. Electrocatalyst approaches and challenges for automotive fuel cells. *Nature* **2012**, *486* (7401), 43–51.
- (23) Hou, J.; Yang, M.; Ke, C.; Wei, G.; Priest, C.; Qiao, Z.; Wu, G.; Zhang, J. Platinum-group-metal catalysts for proton exchange membrane fuel cells: From catalyst design to electrode structure optimization. *J. Energy Chem.* **2020**, 2 (1), No. 100023.
- (24) Qiao, Z.; Wang, C.; Li, C.; Zeng, Y.; Hwang, S.; Li, B.; Karakalos, S.; Park, J.; Kropf, A. J.; Wegener, E. C.; et al. Atomically dispersed single iron sites for promoting Pt and Pt3Co fuel cell catalysts: performance and durability improvements. *Energy Environ. Sci.* 2021, 14 (9), 4948–4960.
- (25) Cullen, D. A.; Neyerlin, K. C.; Ahluwalia, R. K.; Mukundan, R.; More, K. L.; Borup, R. L.; Weber, A. Z.; Myers, D. J.; Kusoglu, A. New roads and challenges for fuel cells in heavy-duty transportation. *Nat. Energy* **2021**, *6* (5), 462–474.
- (26) Akula, S.; Mooste, M.; Zulevi, B.; McKinney, S.; Kikas, A.; Piirsoo, H.-M.; Rähn, M.; Tamm, A.; Kisand, V.; Serov, A.; et al. Mesoporous textured Fe-N-C electrocatalysts as highly efficient cathodes for proton exchange membrane fuel cells. *J. Power Sources* **2022**, 520, No. 230819, DOI: 10.1016/j.jpowsour.2021.230819.
- (27) Adabi, H.; Shakouri, A.; Ul Hassan, N.; Varcoe, J. R.; Zulevi, B.; Serov, A.; Regalbuto, J. R.; Mustain, W. E. High-performing commercial Fe–N–C cathode electrocatalyst for anion-exchange membrane fuel cells. *Nat. Energy* **2021**, *6* (8), 834–843.
- (28) Workman, M. J.; Serov, A.; Tsui, L.-k.; Atanassov, P.; Artyushkova, K. Fe-N-C Catalyst Graphitic Layer Structure and Fuel Cell Performance. ACS Energy Lett. 2017, 2 (7), 1489–1493.
- (29) Woo, J.; Sa, Y. J.; Kim, J. H.; Lee, H. W.; Pak, C.; Joo, S. H. Impact of textural properties of mesoporous porphyrinic carbon electrocatalysts on oxygen reduction reaction activity. *ChemElectroChem* **2018**, *5* (14), 1928–1936, DOI: 10.1002/celc.201800183.
- (30) Zhang, H.; Chung, H. T.; Cullen, D. A.; Wagner, S.; Kramm, U. I.; More, K. L.; Zelenay, P.; Wu, G. High-performance fuel cell cathodes exclusively containing atomically dispersed iron active sites. *Energy Environ. Sci.* **2019**, *12* (8), 2548–2558.
- (31) Xie, J.; Liu, Y.; Li, C.; Fan, L. Mesoporous carbon-based PGM-free catalyst cathodes 2021 Annual Merit Review and Peer Evaluation Meeting 2020.
- (32) He, Y.; Liu, S.; Priest, C.; Shi, Q.; Wu, G. Atomically dispersed metal—nitrogen—carbon catalysts for fuel cells: advances in catalyst design, electrode performance, and durability improvement. *Chem. Soc. Rev.* **2020**, *49* (11), 3484–3524.
- (33) Wang, Q.; Shang, L.; Sun-Waterhouse, D.; Zhang, T.; Waterhouse, G. Engineering local coordination environments and site densities for high-performance Fe-N-C oxygen reduction reaction electrocatalysis. *SmartMat* **2021**, *2* (2), 154–175.
- (34) Jia, Q.; Ramaswamy, N.; Hafiz, H.; Tylus, U.; Strickland, K.; Wu, G.; Barbiellini, B.; Bansil, A.; Holby, E. F.; Zelenay, P.; et al. Experimental Observation of Redox-Induced Fe–N Switching Behavior as a Determinant Role for Oxygen Reduction Activity. *ACS Nano* **2015**, *9* (12), 12496–12505.
- (35) Kramm, U. I.; Herranz, J.; Larouche, N.; Arruda, T. M.; Lefèvre, M.; Jaouen, F.; Bogdanoff, P.; Fiechter, S.; Abs-Wurmbach, I.; Mukerjee, S. Structure of the catalytic sites in Fe/N/C-catalysts for O 2-reduction in PEM fuel cells. *Phys. Chem. Chem. Phys.* **2012**, *14* (33), 11673–11688, DOI: 10.1039/C2CP41957B.
- (36) Artyushkova, K.; Workman, M. J.; Matanovic, I.; Dzara, M. J.; Ngo, C.; Pylypenko, S.; Serov, A.; Atanassov, P. Role of Surface Chemistry on Catalyst/Ionomer Interactions for Transition Metal—Nitrogen—Carbon Electrocatalysts. ACS Appl. Energy Mater. 2018, 1
- (37) Ebner, K.; Clark, A. H.; Saveleva, V. A.; Smolentsev, G.; Chen, J.; Ni, L.; Li, J.; Zitolo, A.; Jaouen, F.; Kramm, U. I.; et al. Time-Resolved Potential-Induced Changes in Fe/N/C-Catalysts Studied by In Situ Modulation Excitation X-Ray Absorption Spectroscopy. *Adv. Energy Mater.* **2022**, *12* (14), No. 2103699.

- (38) Saveleva, V. A.; Ebner, K.; Ni, L.; Smolentsev, G.; Klose, D.; Zitolo, A.; Marelli, E.; Li, J.; Medarde, M.; Safonova, O. V.; et al. Potential-Induced Spin Changes in Fe/N/C Electrocatalysts Assessed by In Situ X-ray Emission Spectroscopy. *Angew. Chem., Int. Ed.* **2021**, 60 (21), 11707–11712.
- (39) Wang, W.; Jia, Q.; Mukerjee, S.; Chen, S. Recent Insights into the Oxygen-Reduction Electrocatalysis of Fe/N/C Materials. *ACS Catal.* **2019**, 9 (11), 10126–10141.
- (40) Jia, Q.; Ramaswamy, N.; Tylus, U.; Strickland, K.; Li, J.; Serov, A.; Artyushkova, K.; Atanassov, P.; Anibal, J.; Gumeci, C.; et al. Spectroscopic insights into the nature of active sites in iron–nitrogen–carbon electrocatalysts for oxygen reduction in acid. *Nano Energy* **2016**, *29*, 65–82.
- (41) Zitolo, A.; Goellner, V.; Armel, V.; Sougrati, M.-T.; Mineva, T.; Stievano, L.; Fonda, E.; Jaouen, F. Identification of catalytic sites for oxygen reduction in iron- and nitrogen-doped graphene materials. *Nat. Mater.* **2015**, *14* (9), 937–942.
- (42) Yang, L.; Cheng, D.; Xu, H.; Zeng, X.; Wan, X.; Shui, J.; Xiang, Z.; Cao, D. Unveiling the high-activity origin of single-atom iron catalysts for oxygen reduction reaction. *Proc. Natl. Acad. Sci. U.S.A.* **2018**, *115* (26), 6626–6631.
- (43) Nabae, Y.; Yuan, Q.; Nagata, S.; Kusaba, K.; Aoki, T.; Takao, N.; Itoh, T.; Arao, M.; Imai, H.; Higashi, K. In situ X-ray absorption spectroscopy to monitor the degradation of Fe/N/C cathode catalyst in proton exchange membrane fuel cells. *J. Electrochem. Soc.* **2021**, *168* (1), No. 014513, DOI: 10.1149/1945-7111/abdc64.
- (44) Saveleva, V. A.; Kumar, K.; Theis, P.; Salas, N. S.; Kramm, U. I.; Jaouen, F.; Maillard, F.; Glatzel, P. Fe–N–C Electrocatalyst and Its Electrode: Are We Talking about the Same Material? *ACS Appl. Energy Mater.* **2023**, *6* (2), 611–616.
- (45) Qadri, S.; Dinderman, M.; Dressick, W.; Schoen, P.; Lubitz, P.; He, J.; Tonucci, R.; Cross, J. Structural and magnetic properties of FeB microfibers. *Appl. Phys. A: Mater. Sci. Process.* **2007**, *89*, 493–496.
- (46) Avakyan, L.; Manukyan, A.; Bogdan, A.; Gyulasaryan, H.; Coutinho, J.; Paramonova, E.; Sukharina, G.; Srabionyan, V.; Sharoyan, E.; Bugaev, L. Synthesis and structural characterization of iron-cementite nanoparticles encapsulated in carbon matrix. *J. Nanopart. Res.* **2020**, 22 (1), No. 30, DOI: 10.1007/s11051-019-4698-8.
- (47) Vankó, G.; Neisius, T.; Molnar, G.; Renz, F.; Karpati, S.; Shukla, A.; De Groot, F. M. Probing the 3d spin momentum with X-ray emission spectroscopy: The case of molecular-spin transitions. *J. Phys. Chem. B* **2006**, *110* (24), 11647–11653.
- (48) Kennedy, B.; Brain, G.; Murray, K. Cholorophthalocyanine iron (III) FePc (-2) Cl. A spin-admixed (S = 32/S = (frsoll 5/2) system. *Inorg. Chim. Acta* 1984, 81, L29–L31.
- (49) Kennedy, B. J.; Murray, K. S.; Zwack, P. R.; Homborg, H.; Kalz, W. Spin states in iron (III) phthalocyanines studied by Moessbauer, magnetic susceptibility, and ESR measurements. *Inorg. Chem.* **1986**, 25 (15), 2539–2545.
- (50) Emamian, S.; Ireland, K. A.; Purohit, V.; McWhorter, K. L.; Maximova, O.; Allen, W.; Jensen, S.; Casa, D. M.; Pushkar, Y.; Davis, K. M. X-ray Emission Spectroscopy of Single Protein Crystals Yields Insights into Heme Enzyme Intermediates. *J. Phys. Chem. Lett.* **2023**, *14*, 41–48.
- (51) Li, J.; Sougrati, M. T.; Zitolo, A.; Ablett, J. M.; Oğuz, I. C.; Mineva, T.; Matanovic, I.; Atanassov, P.; Huang, Y.; Zenyuk, I. Identification of durable and non-durable FeN x sites in Fe-N-C materials for proton exchange membrane fuel cells. *Nat. Catal.* **2021**, 4 (1), 10–19, DOI: 10.1038/s41929-020-00545-2.
- (52) March, A. M.; Assefa, T. A.; Bressler, C.; Doumy, G.; Galler, A.; Gawelda, W.; Kanter, E. P.; Németh, Z.; Pápai, M.; Southworth, S. H. Feasibility of valence-to-core x-ray emission spectroscopy for tracking transient species. *J. Phys. Chem. C* **2015**, *119* (26), 14571–14578, DOI: 10.1021/jp511838q.
- (53) Dale, B.; Williams, R.; Johnson, C.; Thorp, T. S = 1 spin state of divalent iron. I. Magnetic properties of phthalocyanine iron (II). *J. Chem. Phys.* **1968**, 49 (8), 3441–3444.

- (54) Evangelisti, M.; Bartolomé, J.; De Jongh, L.; Filoti, G. Magnetic properties of  $\alpha$ -iron (II) phthalocyanine. *Phys. Rev. B* **2002**, *66* (14), No. 144410.
- (55) Mansour, A. N.; Ko, J. K.; Waller, G. H.; Martin, C. A.; Zhang, C.; Qiao, X.; Wang, Y.; Zhou, X.; Balasubramanian, M. Structural analysis of K4Fe (CN) 6· 3H2O, K3Fe (CN) 6 and prussian blue. ECS J. Solid State Sci. Technol. 2021, 10 (10), No. 103002.
- (56) Oosterhuis, W.; Lang, G. Mössbauer effect in K 3 Fe (CN) 6. *Phys. Rev.* **1969**, *178* (2), 439.
- (57) Champion, A.; Drickamer, H. Effect of pressure on the Mössbauer resonance in potassium ferrocyanide, potassium ferricyanide, and insoluble Prussian blue. *J. Chem. Phys.* **1967**, *47* (8), 2591–2594.
- (58) Glatzel, P.; Bergmann, U. High resolution 1s core hole X-ray spectroscopy in 3d transition metal complexes—electronic and structural information. *Coord. Chem. Rev.* **2005**, 249 (1–2), 65–95.
- (59) Guda, A. A.; Guda, S. A.; Martini, A.; Kravtsova, A.; Algasov, A.; Bugaev, A.; Kubrin, S. P.; Guda, L.; Šot, P.; van Bokhoven, J. A. Understanding X-ray absorption spectra by means of descriptors and machine learning algorithms. *Npj Comput. Mater.* **2021**, 7 (1), No. 203, DOI: 10.1038/s41524-021-00664-9.
- (60) Kiwi, J.; Denisov, N.; Gak, Y.; Ovanesyan, N.; Buffat, P.; Suvorova, E.; Gostev, F.; Titov, A.; Sarkisov, O.; Albers, P. Catalytic Fe3+ clusters and complexes in Nafion active in photo-Fenton processes. High-resolution electron microscopy and femtosecond studies. *Langmuir* **2002**, *18* (23), 9054–9066, DOI: 10.1021/la020648k.
- (61) Ramaswamy, N.; Tylus, U.; Jia, Q.; Mukerjee, S. Activity Descriptor Identification for Oxygen Reduction on Nonprecious Electrocatalysts: Linking Surface Science to Coordination Chemistry. *J. Am. Chem. Soc.* **2013**, *135* (41), 15443–15449.
- (62) Holby, E. F.; Wang, G.; Zelenay, P. Acid stability and demetalation of PGM-free ORR electrocatalyst structures from density functional theory: a model for "single-atom catalyst" dissolution. ACS Catal. 2020, 10, 14527–14539.
- (63) Martynov, A. G.; Mack, J.; May, A. K.; Nyokong, T.; Gorbunova, Y. G.; Tsivadze, A. Y. Methodological survey of simplified TD-DFT methods for fast and accurate interpretation of UV-vis-NIR spectra of phthalocyanines. *ACS Omega* **2019**, *4* (4), 7265–7284.
- (64) Martinez, U.; Komini Babu, S.; Holby, E. F.; Chung, H. T.; Yin, X.; Zelenay, P. Progress in the development of Fe-based PGM-free electrocatalysts for the oxygen reduction reaction. *Adv. Mater.* **2019**, 31 (31), No. 1806545, DOI: 10.1002/adma.201806545.
- (65) Serov, A.; Atanassov, P. B. Carbendazim-based catalytic materials. WO2014011831A1, 2016.
- (66) Serov, A.; Halevi, B.; Robson, M.; Patterson, W.; Artyushkova, K.; Atanassov, P. B. Cathode catalysts for fuel cell application derived from polymer precursors. US20150295248A1, 2016.
- (67) Ravel, B.; Newville, M. ATHENA, ARTEMIS, HEPHAESTUS: data analysis for X-ray absorption spectroscopy using IFEFFIT. *J. Synchrotron Radiat.* **2005**, *12*, 537–541.
- (68) Rehr, J. J.; Albers, R. C. Theoretical approaches to x-ray absorption fine structure. *Rev. Mod. Phys.* **2000**, *72*, 621.
- (69) Leshchev, D.; Rakitin, M.; Luvizotto, B.; Kadyrov, R.; Ravel, B.; Attenkofer, K.; Stavitski, E. The Inner Shell Spectroscopy beamline at NSLS-II: a facility for in situ and operando X-ray absorption spectroscopy for materials research. *J. Synchrotron Radiat.* **2022**, 29 (4), 1095–1106.
- (70) Jensen, S. C.; Sullivan, B.; Hartzler, D. A.; Pushkar, Y. DIY XES—development of an inexpensive, versatile, and easy to fabricate XES analyzer and sample delivery system. *X-Ray Spectrom.* **2019**, 48 (5), 336–344.